

Modeling for compression of field-reversed configurations by an imploding liner

Xiaoguang Wang, Guanqiong Wang, Bin Liu, Lulu Li, and Xianjun Yang

Citation: *Physics of Plasmas* **23**, 112706 (2016); doi: 10.1063/1.4968238

View online: <http://dx.doi.org/10.1063/1.4968238>

View Table of Contents: <http://scitation.aip.org/content/aip/journal/pop/23/11?ver=pdfcov>

Published by the AIP Publishing

Articles you may be interested in

[Hybrid equilibria of field-reversed configurations](#)

Phys. Plasmas **18**, 112509 (2011); 10.1063/1.3660674

[Review of field-reversed configurations](#)

Phys. Plasmas **18**, 070501 (2011); 10.1063/1.3613680

[Equilibrium rotation in field-reversed configurations](#)

Phys. Plasmas **15**, 012505 (2008); 10.1063/1.2834271

[A high density field reversed configuration \(FRC\) target for magnetized target fusion: First internal profile measurements of a high density FRC](#)

Phys. Plasmas **11**, 2580 (2004); 10.1063/1.1689666

[A magnetohydrodynamic model of rotating magnetic field current drive in a field-reversed configuration](#)

Phys. Plasmas **7**, 4135 (2000); 10.1063/1.1290279



**COMPLETELY
REDESIGNED!**



Physics Today Buyer's Guide
Search with a purpose.

Modeling for compression of field-reversed configurations by an imploding liner

Xiaoguang Wang,¹ Guanqiong Wang,¹ Bin Liu,² Lulu Li,^{1,2} and Xianjun Yang^{1,2}

¹Center for Fusion Energy Science and Technology, Chinese Academy of Engineering Physics, Beijing 100088, China

²Institute of Applied Physics and Computational Mathematics, Beijing 100094, China

(Received 2 September 2016; accepted 7 November 2016; published online 28 November 2016)

This article proposes a one-dimensional physical model to investigate the compression of reversed-field configurations (FRCs) by an imploding cylindrical liner. In this model, axial contraction of FRCs is included and parallel thermal conduction is considered as well as the radial, approximately in the open field line region of FRCs. Comparison with Spencer's analytic model of FRCs adiabatic compression shows similar results. Modeling results also indicate that classical transport model is preferred in the magnetized target fusion regime and axial contraction plays an important role in the dynamics of compression of FRCs using an imploding liner. *Published by AIP Publishing.*
[\[http://dx.doi.org/10.1063/1.4968238\]](http://dx.doi.org/10.1063/1.4968238)

I. INTRODUCTION

Magneto-inertial fusion (MIF) approaches utilize an embedded magnetic field to improve the plasma energy confinement, reducing the required implosion velocity and the density-radius product relative to conventional inertial confined fusion (ICF).^{1–5} Magnetic target fusion (MTF) is one of the MIF concepts.^{6–13} In MTF, one uses an imploding conducting liner to compress the field-reversed configurations (FRCs) to fusion conditions.^{11,14,15} The formation,^{14,16} translation,¹⁵ and capture of FRCs and the implosion of aluminum liner driven by electromagnetic pulse power¹¹ have been demonstrated for this kind of MTF. Although compression experiments of FRCs by using an imploding liner were performed successfully, yet the signature of plasma compression was weak.¹⁷ The study on compression of FRCs is essential for further research of MTF.

Earlier, Spencer proposed an analytic model to investigate the adiabatic compression of FRCs.¹⁸ Many experiments and analytical analyses were also conducted for the magnetic-flux and axial compression of FRCs, respectively.^{19–21} One two-dimensional magnetohydrodynamic (MHD) simulation showed that the FRCs could be compressed and heated effectively up to multi-keV and $\sim 10^3$ times of initial density by using an imploding cylindrical aluminum liner.¹¹ However, one-dimensional physical model is more appropriate for scaling study and investigation of physical effects compared with analytic (zero-dimensional) and two-dimensional models where the physical effects are kept as many as possible.

The radial one-dimensional equilibrium approximation of FRCs is valid if the elongation E is large enough, i.e., $E \gg 1$.^{22–24} Since FRCs with $E = 6–7$ are generally chosen as the magnetized target for MTF. Considering the implosion of cylindrical liner only, one-dimensional physical model is appropriate for investigating the compression of FRCs. However, FRCs will contract in the axial direction due to increasing magnetic stress force at two sides during

compression by using an imploding liner. Furthermore, the axial contraction (AC) motion is significant according to analytical and two-dimensional simulation results.^{11,18} It is found that the axial motion is coupled with the radial one for adiabatic compression of FRCs according to Spencer's analytic model.¹⁸ Therefore, one could analytically describe the axial motion of FRCs with radial convergence velocity instead of the axial momentum equation.

Generally, there is a large axial heat flux flowing toward the ends of the chamber along magnetic fields in the open field line region, and the axial heat flux is far larger than the radial one, especially in scrape-off layer (SOL). Therefore, the thermal conduction parallel to the axial magnetic field must be considered as well as the radial thermal conduction in the open field line region.

In this paper, a one-dimensional physical model is proposed for investigation on the compression of FRCs using an imploding liner, including both the effects of axial contraction and parallel thermal conduction besides others. The physical model is derived and described in Section II. Sec. III presents the modeling results. Finally, the conclusion is given in Sec. IV.

II. PHYSICAL MODEL

FRC is a compact torus which has closed magnetic surfaces. Fig. 1 presents the diagram of cross section structure of FRCs, where r_s is the separatrix radius, r_w is the inner radius of liner, and l_s is the length of FRCs. There is closed poloidal magnetic force lines inside the separatrix. Outside and close to the separatrix is a thin plasma region called scrape-off layer (SOL) where the magnetic lines are open. Generally, the thickness of SOL is $\delta r \sim \rho_{i0}$ where $\rho_{i0} = 2m_i T_0^{1/2} / (qB_e)$ is the ion “external” Larmor radius.²⁵ In the SOL, heat and particle flux from the plasma region will flow fast toward the ends of chamber along the open force lines, and cannot approach the wall of liner. Thus, there is an approximate vacuum region between the metal shell (liner)

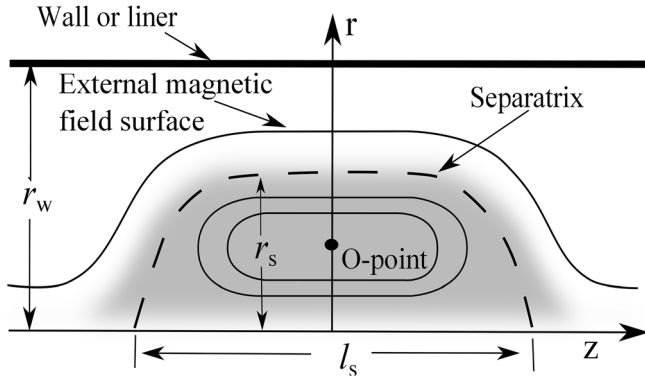


FIG. 1. The diagram of cross section structure for FRCs. Here r_s is the separatrix radius, r_w is the inner radius of liner, and l_s is the length of FRCs.

and the SOL. The magnetic field is uniform and open in the vacuum region. Only the implosion of the cylindrical liner is considered here.

Fig. 2 gives an overview of the physical model for the compression of FRCs by using an imploding liner. It is separated into four regions in radial direction. The first is plasma region for $r < r_s$. It is found that FRCs will contract in the axial direction during wall or flux compression.^{11,18} Therefore, the axial motion as well as the radial must be considered in the first region. Because of closed and straight magnetic lines around the middle plane, the parallel thermal conductions of electrons and ions are ignored in this region. The second is SOL region for $r_s + \delta r > r > r_s$. The third is vacuum magnetic field region for $r_w > r > r_s + \delta r$. In the open field line region ($r_w > r > r_s$), both parallel and transverse thermal conductions need to be included. The last is aluminum liner region for $R > r > r_w$ where R is the outer radius of liner. The thickness of liner is $L_t = R - r_w$. The low density and temperature plasma is employed to simulate the vacuum region here. In addition, the liner is also described in terms of the fluid method.

The hydrodynamic control equations mainly include the continuum equation, momentum equation, and electron and ion energy equations.^{26–28} In cylindrical coordinates, it is uniform in θ direction. The rotation of FRC is not taken into

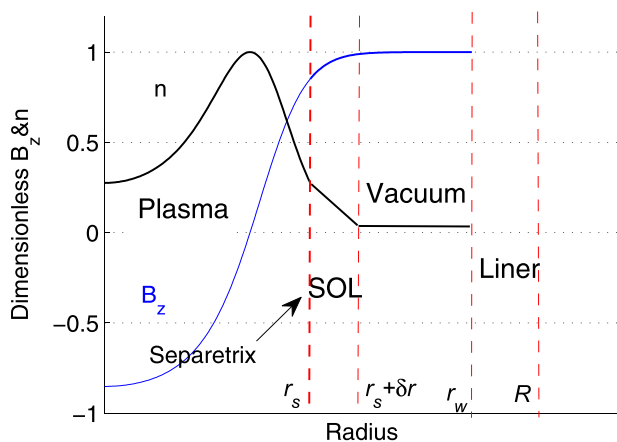


FIG. 2. Schematic overview of the physical model of compression of FRCs by using an imploding liner. It is separated into four regions in radial direction: the plasma region, the SOL, the vacuum region, and the liner region.

account. And only the axial magnetic field is included. The radial motion equation is written by

$$\rho \frac{\partial u_r}{\partial t} + \rho u_r \frac{\partial u_r}{\partial r} = -\frac{\partial}{\partial r} \left(P_e + P_i + \frac{B_z^2}{8\pi} \right) + \frac{\partial}{\partial r} \left[\nu_{sr} \frac{1}{r} \frac{\partial}{\partial r} (u_r r) \right] + \frac{1}{r^2} \frac{\partial}{\partial r} \left[r^3 \nu_{tr} \frac{\partial}{\partial r} \left(\frac{u_r}{r} \right) \right] \quad (1)$$

for all regions where ρ is the mass density, and ν_{sr} and ν_{tr} are the coefficients of ion viscosity.

Applying rigid-rotor equilibrium model and adiabatic compression assumption, the evolution of FRC's length l_s for wall or flux compression is derived as¹⁸

$$\frac{dl_s}{l_s} = \frac{(4-2\gamma)}{\gamma} \frac{dr_w}{r_w} + \frac{2(3-\gamma-\epsilon)}{\gamma} \frac{dx_s}{x_s} - \frac{(1+\epsilon-\gamma\epsilon)}{\gamma} \frac{d\beta}{\beta}, \quad (2)$$

where x_s is the ratio of separatrix radius r_s to inner radius of liner r_w and $\langle\beta\rangle$ is the average magnetic pressure ratio (or normalized pressure) written by

$$x_s = r_s/r_w \quad (3)$$

and

$$\langle\beta\rangle = 1 - \frac{x_s^2}{2} \quad (4)$$

respectively. Here γ is the adiabatic coefficient, $\gamma = 5/3$ for adiabatic compression here. $\epsilon = (x_s/f)(df/dx_s)$ is a radial profile parameter varying from -1 to 0 , where $f = x_s / \int_0^1 (1-\beta)^{1/2} du$, and $u = 2r^2/r_s^2 - 1$.¹⁸ f is only a function of x_s . And $\beta = p(u)/p_m$ is the magnetic pressure ratio (normalized pressure). ϵ , generally doesn't determine the modeling results for the wall compression, so we set it as constant for simplicity. Since the rigid-rotor equilibrium model, whose poloidal flux is close to that of the high-flux sharp boundary (HFSB) profile, is chosen as the initial profile condition, $\epsilon = 0$ (HFSB) is given in the following. The time derivative of ϵ , however, must be taken into account strictly for the flux compression of FRCs.

The axial velocities at sides of FRC $u_{zs\mp}$ are derived from Eq. (8) as

$$\begin{aligned} \frac{u_{zs\mp}}{l_s} &= \pm \frac{1}{2} \frac{dl_s}{l_s dt} \\ &= \pm \frac{1}{2} \left[\frac{(4-2\gamma)}{\gamma} \frac{dr_w}{r_w dt} + \frac{2(3-\gamma-\epsilon)}{\gamma} \frac{dx_s}{x_s dt} - \frac{(1+\epsilon-\gamma\epsilon)}{\gamma} \frac{d\langle\beta\rangle}{\langle\beta\rangle dt} \right], \end{aligned} \quad (5)$$

where the \pm signs indicate two sides, respectively. The radial velocity at inner wall of liner is $u_{rw} = dr_w/dt$. The radial velocity at separatrix is $u_{rs} = dr_s/dt$. Omitting the subscript \mp and \pm signs, the axial velocities at sides are expressed as

$$u_{zs} = \frac{1}{2} l_s \left[\frac{(4-2\gamma) u_{rw}}{\gamma} \frac{r_w}{r_w} + \frac{2(3-\gamma-\epsilon)}{\gamma} \frac{(r_w u_{rs} - r_s u_{rw})}{r_s r_w} \right. \\ \left. + \frac{(1+\epsilon-\gamma\epsilon)}{\gamma} \frac{(r_w u_{rs} - r_s u_{rw}) x_s}{\langle \beta \rangle r_w^2} \right]. \quad (6)$$

The axial contraction velocity at middle plane is $u_{zm} = 0$ as a result of the symmetry. It is found from one-dimensional numerical calculation without axial contraction that the distribution of radial contraction velocity is linear during compression of FRC. It is believed that the physical mechanism and process of axial contraction are the same with that of radial compression. It is assumed that the distribution of axial contraction velocity is also linear. The gradient of axial contraction velocity is written approximately by

$$\frac{\partial u_z}{\partial z} = \frac{u_{zs} - u_{zm}}{l_s/2} = \frac{2u_{zs}}{l_s} \quad (7)$$

for $r < r_s$. The axial velocity is

$$u_z = 0 \quad (8)$$

for $r > r_s$ since there is no axial contraction in open field line region. Eqs. (6)–(8) describe the axial motion of FRCs.

It is assumed that the density is uniform in axial direction. Applying Eqs. (7) and (8), the continuum equation Eq. (1) is written by

$$\begin{cases} \frac{\partial \rho}{\partial t} + \frac{1}{r} \frac{\partial}{\partial r} (\rho u_r r) + \rho \frac{2u_{zs}}{l_s} = 0 & (r < r_s) \\ \frac{\partial \rho}{\partial t} + \frac{1}{r} \frac{\partial}{\partial r} (\rho u_r r) = 0 & (r > r_s). \end{cases} \quad (9)$$

Then the compression work term of the electron energy equation is written by

$$\frac{P_e}{\rho} \nabla \cdot \mathbf{u} = \frac{P_e}{\rho} \frac{1}{r} \frac{\partial}{\partial r} (u_r r) + \frac{P_e}{\rho} \frac{\partial u_z}{\partial z} = \frac{P_e}{\rho} \frac{1}{r} \frac{\partial}{\partial r} (u_r r) + \frac{P_e}{\rho} \frac{2u_{zs}}{l_s} \quad (10)$$

in plasma region $r < r_s$. For regions $r > r_s$, it is written by

$$\frac{P_e}{\rho} \nabla \cdot \mathbf{u} = \frac{P_e}{\rho} \frac{1}{r} \frac{\partial}{\partial r} (u_r r) \quad (11)$$

without axial contraction. The thermal conduction term is

$$\nabla \cdot (\kappa_e \nabla T_e) = \kappa_{er} \frac{1}{\rho r} \frac{\partial}{\partial r} \left[\frac{\partial}{\partial r} (T_e r) \right] \quad (12)$$

in plasma region $r < r_s$, where κ_{er} is the coefficient of radial electron thermal conduction. In regions $r > r_s$, the term of electron thermal conduction is written by

$$\nabla \cdot (\kappa_e \nabla T_e) = \kappa_{er} \frac{1}{\rho r} \frac{\partial}{\partial r} \left[\frac{\partial}{\partial r} (T_e r) \right] + \kappa_{ez} \frac{T_e}{l_s^2} \quad (13)$$

including the parallel thermal conduction, where κ_{ez} is the coefficient of parallel electron thermal conduction. By applying Eqs. (10)–(13), the electron energy equation is written by

$$\frac{\partial \varepsilon_e}{\partial t} + u_r \frac{\partial \varepsilon_e}{\partial r} = -\frac{P_e}{\rho} \left[\frac{1}{r} \frac{\partial}{\partial r} (u_r r) + \frac{2u_{zs}}{l_s} \right] \\ + \kappa_{er} \frac{1}{\rho r} \frac{\partial}{\partial r} \left[\frac{\partial}{\partial r} (T_e r) \right] + \frac{\eta_{rt}}{\rho} \left(\frac{c}{4\pi} \frac{\partial B_z}{\partial r} \right)^2 \\ - \chi_{ei} (T_e - T_i) - \chi_{er} T_e + Q_e \quad (r < r_s) \quad (14a)$$

and

$$\frac{\partial \varepsilon_e}{\partial t} + u_r \frac{\partial \varepsilon_e}{\partial r} = -\frac{P_e}{\rho} \frac{1}{r} \frac{\partial}{\partial r} (u_r r) + \kappa_{er} \frac{1}{\rho r} \frac{\partial}{\partial r} \left[\frac{\partial}{\partial r} (T_e r) \right] \\ + \frac{\kappa_{ez} T_e}{\rho l_s^2} + \frac{\eta_{rt}}{\rho} \left(\frac{c}{4\pi} \frac{\partial B_z}{\partial r} \right)^2 - \chi_{ei} (T_e - T_i) \\ - \chi_{er} T_e + Q_e \quad (r > r_s), \quad (14b)$$

where ε_e is the electron specific internal energy, η_{rt} is the electron transverse resistivity, χ_{ei} is the relaxation coefficient of electron-ion temperature, and χ_{er} is the coefficient of radiation.

The work of axial component of viscous stress is ignored here. In a similar way, the ion energy equation is written by

$$\frac{\partial \varepsilon_i}{\partial t} + u_r \frac{\partial \varepsilon_i}{\partial r} = -\frac{P_i}{\rho} \left[\frac{1}{r} \frac{\partial}{\partial r} (u_r r) + \frac{2u_{zs}}{l_s} \right] + \frac{\nu_{sr}}{\rho} \left[\frac{1}{r} \frac{\partial}{\partial r} (u_r r) \right]^2 \\ + \frac{\nu_{tr}}{\rho} \left[r \frac{\partial}{\partial r} \left(\frac{u_r}{r} \right) \right]^2 + \kappa_{ir} \frac{1}{\rho r} \frac{\partial}{\partial r} \left[\frac{\partial}{\partial r} (T_i r) \right] \\ + \chi_{ei} (T_e - T_i) + Q_i \quad (r < r_s) \quad (15a)$$

and

$$\frac{\partial \varepsilon_i}{\partial t} + u_r \frac{\partial \varepsilon_i}{\partial r} = -\frac{P_i}{\rho} \frac{1}{r} \frac{\partial}{\partial r} (u_r r) + \frac{\nu_{sr}}{\rho} \left[\frac{1}{r} \frac{\partial}{\partial r} (u_r r) \right]^2 \\ + \frac{\nu_{tr}}{\rho} \left[r \frac{\partial}{\partial r} \left(\frac{u_r}{r} \right) \right]^2 + \kappa_{ir} \frac{1}{\rho r} \frac{\partial}{\partial r} \left[\frac{\partial}{\partial r} (T_i r) \right] \\ + \frac{\kappa_{iz} T_i}{\rho l_s^2} + \chi_{ei} (T_e - T_i) + Q_i \quad (r > r_s), \quad (15b)$$

where κ_{ir} and κ_{iz} are the coefficients of radial and parallel ion thermal conduction, respectively. The fourth and fifth terms are the work of radial component of viscous stress at the right side of Eq. (15a). The ideal equation of state is applied in plasma, SOL, and vacuum regions. The liner's equation of state is considered by using a table of EOS.²⁷

The evolution equation of magnetic field is written by

$$\frac{\partial B_z}{\partial t} + \frac{1}{r} \frac{\partial}{\partial r} (B_z u_r r) = \frac{c^2}{4\pi r} \frac{\partial}{\partial r} \left(r \eta_{rt} \frac{\partial B_z}{\partial r} \right), \quad (16)$$

in all regions. Eqs. (1), (6)–(9), and (14)–(16) are the control equations of the physical model. In all the formulas, CGS units are used. Note that both effects of resistivity dissipation and ohmic heating are included in the liner region. The resistivity dissipation time (about 17 ms) in liner is far larger than the implosion time (about 20 μ s) here. But the wall melting and impurity release are not taken into account in this paper.

The coefficients of electron and ion thermal conduction are given by Refs. 26 and 29, respectively. If the Bohm regime is employed, the coefficients of radial thermal conduction are given by

$$\kappa_{er} = \begin{cases} \frac{n_e T_e \tau_e}{m_e} \frac{x_e^2 \Gamma_{1,1} + \Gamma_{1,2}}{x_e^4 + x_e^2 \Gamma_{7,1} + \Gamma_{7,2}^2} & (x_e < 1) \\ \frac{c T_e}{6 e B} & (x_e > 1) \end{cases} \quad (17)$$

and

$$\kappa_{ir} = \begin{cases} \frac{n_i T_i \tau_i}{m_i} \frac{2x_i^2 + 2.645}{x_i^4 + 2.70x_i^2 + 0.677} & (x_i < 1) \\ \frac{c T_i}{6 e B} & (x_i > 1), \end{cases} \quad (18)$$

where $x_e = \omega_{ce} \tau_e$ and $x_i = \omega_{ci} \tau_i$, ω_{ce} and ω_{ci} are the electron and ion cyclotron frequencies, τ_e and τ_i are the electron and ion collision times, respectively. $\Gamma_{i,j}$ is dimensionless coefficient. The relaxation coefficient of electron-ion temperature χ_{ei} , the transverse electron resistivity η_{rt} and the viscous coefficients ν_{tr} and ν_{cr} are given following Ref. 29. The radiative coefficient χ_{er} is given by Ref. 27. The model will return to one-dimensional case without the axial contraction and parallel thermal conduction when $u_{zs} = 0$ for $r < r_s$ and $\kappa_{zi,e} = 0$ for $r > r_s$.

The pulse current to drive liner is expressed in terms of a time-dependent sine function $I = I_{max} \sin(t\pi/2T)$ where T is the rising period of pulse current, and I_{max} is the maximum driven current. For simplicity, we set the boundary condition of the axial magnetic field as the electromagnetic pulse drive source

$$B_{zb} = \frac{2}{c} I / R = \frac{2}{c} I_{max} \sin(t\pi/2T) / R. \quad (19)$$

The physical model derived above is solved numerically by using a Lagrange, one-dimensional MHD code DEIRA.^{27,28,30} The benchmark of DEIRA code was done in the MTF regime. Previous experiment and simulation, where the 1.36 T vacuum magnetic field was compressed to 540 T by an imploding aluminum liner,¹⁷ was repeated very well by using DEIRA code.

The rigid-rotor equilibrium model is employed as the initial profile of numerical simulation. So the initial profiles are

$$B_z = B_e \tanh[K(2r^2/r_s^2 - 1)] \quad (20a)$$

$$n = n_m \operatorname{sech}^2[K(2r^2/r_s^2 - 1)] \quad (20b)$$

and uniform temperature $T_i = T_e$ in plasma region. In SOL region, the initial profiles are

$$B_z = B_e (1 - \tanh K) * \exp(-(r - r_s)/\delta r) \quad (21a)$$

and

$$n = n_m + (n_{vac} - n_m \operatorname{sech}^2 K) * (r/r_s)^p, \quad (21b)$$

where n_{vac} is the density in vacuum region and p is the upper index related to density profile. The magnetic field and density is uniform in radial direction

$$B_z = B_e \quad (22a)$$

and

$$n = n_{vac} \quad (22b)$$

in vacuum region. The initial profiles are

$$B_z = B_e \quad (23a)$$

and

$$n = n_l \quad (23b)$$

in liner region where n_l is the number density of liner. K is the geometry factor of the profile in rigid-rotor equilibrium model which is calculated by³¹

$$\tanh K / K = 1 - \frac{1}{2} x_s^2. \quad (24)$$

III. MODELING RESULTS

A. Comparison with analytic model

In order to demonstrate the availability, we compared the one-dimensional model with an analytic model of adiabatic wall compression of FRCs in the MTF regime. Following Spencer's analytic model, the wall compression of FRCs could be described by¹⁸

$$l_s \propto r_w^{(4-2\gamma)/\gamma}, \quad T \propto r_w^{-4(\gamma-1)/\gamma}, \quad n_m \propto r_w^{-4\gamma}, \quad B_e \propto r_w^{-2}, \quad (25)$$

where B_e is the external magnetic field (the vacuum magnetic field), n_m is the number density at O-point (the field null point inside the separatrix), γ is the adiabatic coefficient, and $\gamma = 5/3$ here is for adiabatic compression.

The effects of thermal conduction, radiation, and resistivity are not included first in the simulation except for the relaxation of electron-ion temperature for the comparison of one-dimensional model and analytic model. The viscous coefficients are also included for numerical stability. The influence of viscosity on results is ignorable according to calculation. For simplicity, Eq. (21) is also reduced to $B_z = B_e$ and $n = n_{vac}$ for $r_s + \delta r > r > r_s$ in this section. The temperature is approximately uniform for FRCs. The main parameters listed in Table I were chosen from a MTF design.³² Fig. 3 presents the initial equilibrium profile (a) and the numerical one (b) from calculation without pulse driven current. The initial equilibrium changed a little after calculation for an interval of time as Fig. 3(b) shows. Then the pulse current is turned on to drive the liner.

Figs. 4–7 show the simulation results for adiabatic compression of FRCs by using an imploding liner. Fig. 4(a) presents the evolution of liner's inner and outer radius as a function of time. Figs. 4(b)–4(d) show the external magnetic

TABLE I. The main parameters of the compression of FRCs by an imploding aluminum liner.

Liner	r_w	4.4 cm
	L_t	0.07 cm
	ρ	2.7 g/cm ³
FRC	$T_e = T_i$	0.1 keV
	n_m	1×10^{17} cm ⁻³
	Ratio of D/T	1/1
	B_e	2.84 T
	r_s	2.8 cm
	l_s	27 cm
Pulse current	I_{\max}	7 MA
	T	10 μ s

field B_e , the ion temperature T_{im} and density ρ_m at O-point (the field null point inside the separatrix) as a function of time (solid lines) and the corresponding analytical results (AR) (dashed lines). The analytical results are calculated from Eq. (25), where the convergence ratio of FRC $f_{cr} = r_w/r_{w0}$ is from the numerical calculation. It is found that the modeling results are consistent with the analytical ones qualitatively. However, there is a small difference of 10% or so between them at peak compression. The maximum imploding velocity is -0.3 cm/ μ s at the inner surface of the liner according to numerical simulation.

Fig. 5 depicts the evolution of x_s as a function of time for the numerical results corresponding to Fig. 4. It is seen that the x_s increases by about 10% at stagnation. But the change of x_s is not considered in the Spencer's model due to wall compression and assumption of rigid-rotor equilibrium model.¹⁸ It is known from Eqs. (4) and (24) that the shapes of FRC's magnetic field and density profiles are related to x_s . The changing of shapes of FRC's profiles maybe accounts for the distinction between numerical and analytical results. Furthermore, the temperature is also assumed to be uniform in Spencer's model. So the non-uniform distribution of temperature in the simulation may also contribute to the difference as Figs. 3 and 6 show.

The radial velocities as a function of radius are plotted in Fig. 7 corresponding to the acceleration, inertia, stagnation, and rebounding phases, respectively. It is found that the profile of radial velocity is almost linear. Even if the velocity is non-linear distribution for some time at stagnation phase, it is very small as Fig. 7(c) shows. In some way, this result

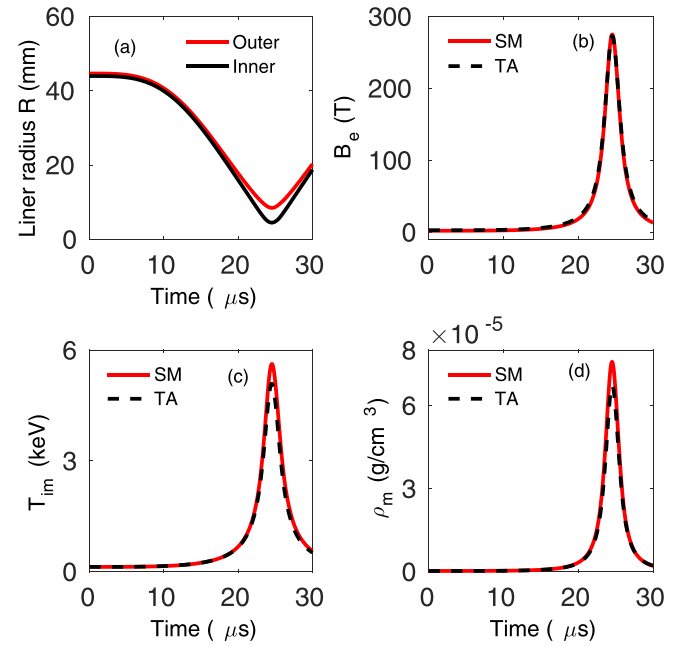


FIG. 4. The inner and the outer radius of liner (a) are plotted as a function of time. The external magnetic field B_e (b), and the ion temperature T_{im} (c) and density ρ_m (d) at the O-point are shown as a function of time for the simulation (SM) (solid lines) and the theoretical analysis (TA) (dashed lines), respectively. The results of SM are consistent with TA qualitatively. A small difference exists about 10% at peak compression.

demonstrates the reasonability of the approximation that the distribution of axial velocity is linear.

The difference between numerical (NR) and analytical results (AR) is defined as

$$f = \frac{X_{NR} - X_{AR}}{X_{AR}} \times 100\%. \quad (26)$$

Other parameters corresponding to Fig. 4, the effect of the maximum imploding velocity as well as the thickness of liner on the physical model is studied. Fig. 8 presents the difference of T_{im} and ρ_m at O-point, B_e and x_s between NR and AR as a function of the maximum imploding velocity U at peak compression. It is found the difference of T_{im} and B_e increases with U . The difference of ρ_m , however, decreases with U . According to calculation, it is observed that the difference of T_{im} increase more than plasma pressure P_m at the O-point (approximately equal to the square of external

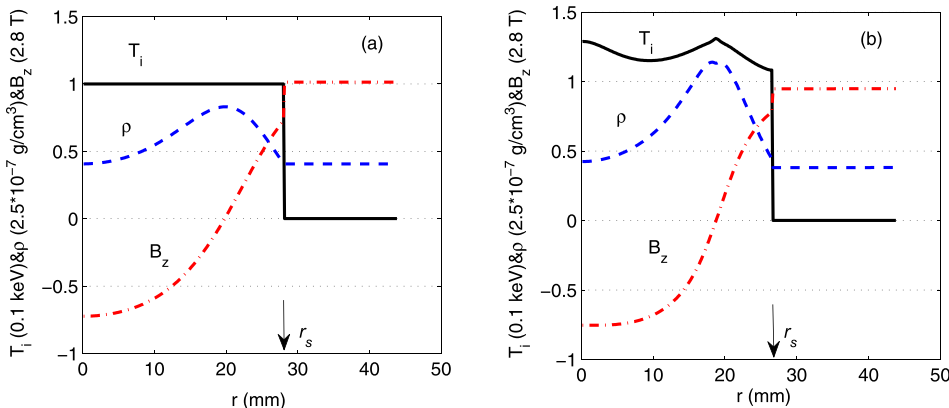
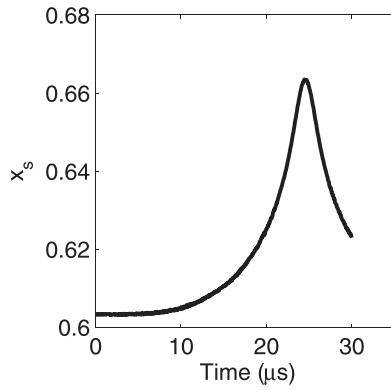


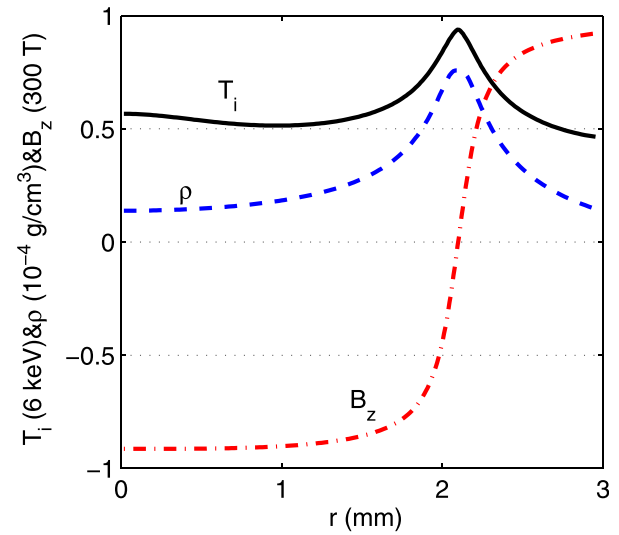
FIG. 3. (a) Shows the initial profiles of T_i , n , and B_z ; (b) gives the corresponding equilibrium profile after calculation for an interval of time without pulse power.

FIG. 5. Corresponding to Fig. 4, the x_s is plotted as a function of time.

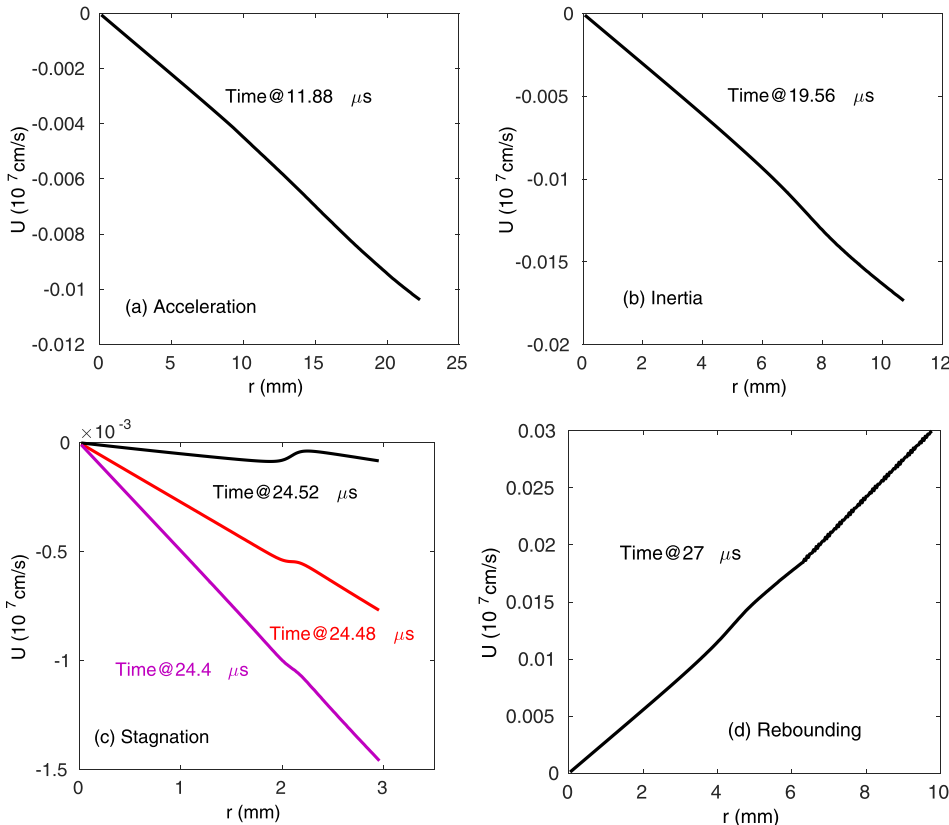
magnetic field B_e) with U , leading to decrease of the difference of ρ_m . The x_s at peak compression also increase with the maximum imploding velocity (i.e., convergence ratio). In addition, the distribution of temperature is more peak around the O-point. Consequently, the shape of FRC's profiles changed more with larger maximum imploding velocity, accounting for the increasing difference. The similar phenomena is also found for changing liner's thickness.

B. Transport model

Corresponding to Fig. 4, Eqs. (20)–(24) were chosen as the initial profile conditions. We turned on the effects of radiation (R), electric resistivity (O), and classical radial (Cr) and parallel (Cz) thermal conductions sequentially in the simulation. Then the Bohm regime was employed only in the SOL region (B2) and in both SOL and plasma regions (B12),

FIG. 6. Corresponding to Fig. 4, the ion temperature T_i , ρ , and B_z are shown as a function of radius at peak compression for $r < r_s$.

respectively. Fig. 9 shows the profiles of T_i , ρ , and B_z at peak compression for different cases. It is found that the profile of magnetic field approaches to rigid-rotor equilibrium model after including the effect of electric resistivity. Besides, the effect of ohmic heating also contributes to the increasing of temperature substantially. In addition, the temperature will become flattened inside the separatrix as a result of the radial thermal conduction effect. A temperature peak appears at the interface between the main plasma and SOL regions after including the effects of radial thermal conduction and electric resistivity. But it will disappear after including the effect

FIG. 7. Corresponding to acceleration (a), inertia (b), stagnation (c) and rebounding (d) phase in Fig. 4, the radial velocities are plotted as a function of radius for $r < r_s$, respectively.

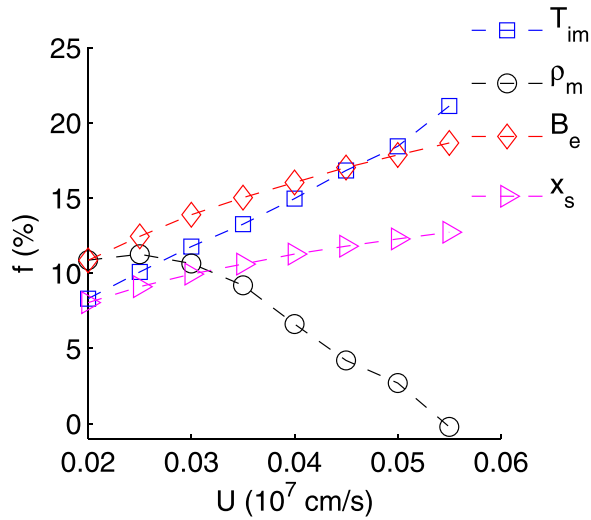


FIG. 8. Other parameters corresponding to Fig. 4, the difference between numerical and analytical results as a function of the maximum imploding velocity U is given for the ion temperature T_{im} and mass density ρ_m at the O-point, external field B_e and x_s at peak compression, respectively.

of parallel thermal conduction in SOL, since the heat from the plasma region will flow away fast along the open lines. It is essential to consider the effect of parallel thermal conduction.

It is found from Fig. 10(a) that the compression work (black line) is much larger than the energy loss due to transport and radiation for case (R, O, B2, Cz). Note that the green and red lines are hidden and covered by other liners because of its small level in Fig. 10(a), and the green line is hidden in Fig. 10(b). In this situation, the adiabatic approximation is valid. However, the adiabatic approximation is questionable if the Bohm transport dominates inside the separatrix, case (R, O, B12, Cz), as Fig. 10(b) shows. But the drift instabilities, which lead to anomalous transport, may be stable because of flat temperature profile inside the separatrix.^{24,33} Considering the non-physical profile of temperature for the case (R, O, B12, Cz), it is concluded that the classical (radial and parallel) transport model is an appropriate choice for the physical model in MTF regime.

C. Comparison of modeling results

The modeling results are compared with a one-dimensional case without the effect of axial contraction.

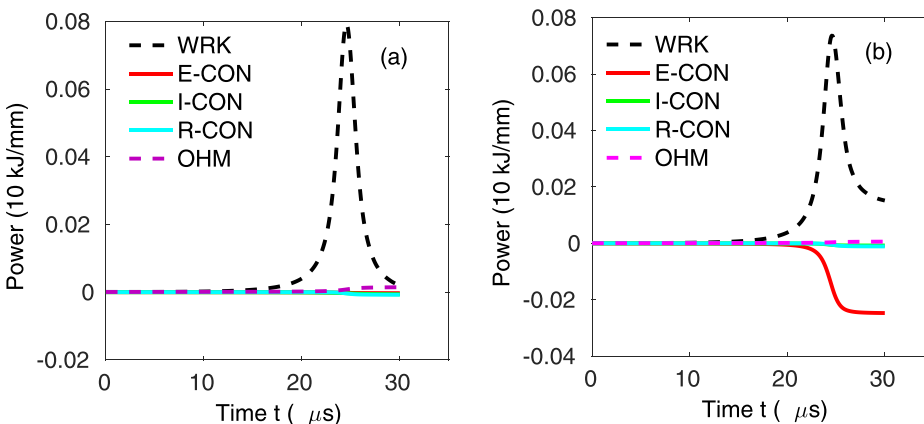


FIG. 10. Corresponding to cases (R,O,B2,Cz) (a) and (R,O,B12,Cz) (b) in Fig. 9, respectively, the compression work and energy loss (color lines) are plotted as a function of time for the plasma region $r < r_s$. Here WRK stands for the compression work (black dashed line), E-CON for the electron thermal conduction loss (red line), I-CON for the ion thermal conduction loss (green line), R-CON for radiative loss (cyan line), OHM for the Ohm heating (purple dashed line).

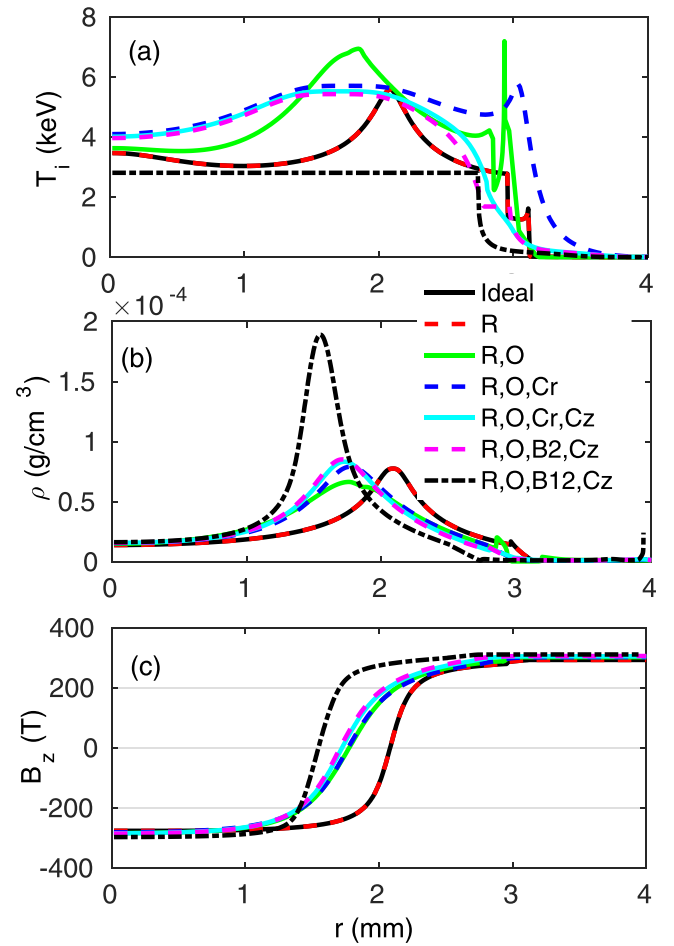


FIG. 9. Corresponding to Fig. 4, the effects of radiation (R), electric resistivity (O), classical radial (Cr), and parallel (Cz) thermal conduction are turned on sequentially. Then the Bohm transport coefficients (Eqs. (26) and (27)) are applied only in SOL (B2) and in both SOL and plasma regions (B12), respectively. The radial profiles of T_i (a), ρ (b), and B_z (c) are presented at peak compression for different cases.

Other parameters corresponding to case (R, O, Cr, Cz) in Fig. 10, Fig. 11 depicts the radial profiles of temperature, density, and magnetic fields at peak compression for including and not including the axial contraction (AC), respectively. It is seen from Fig. 11, in contrast to expectation, that the temperature and density are lower for including the axial contraction than not including because of smaller radial convergence ratio.

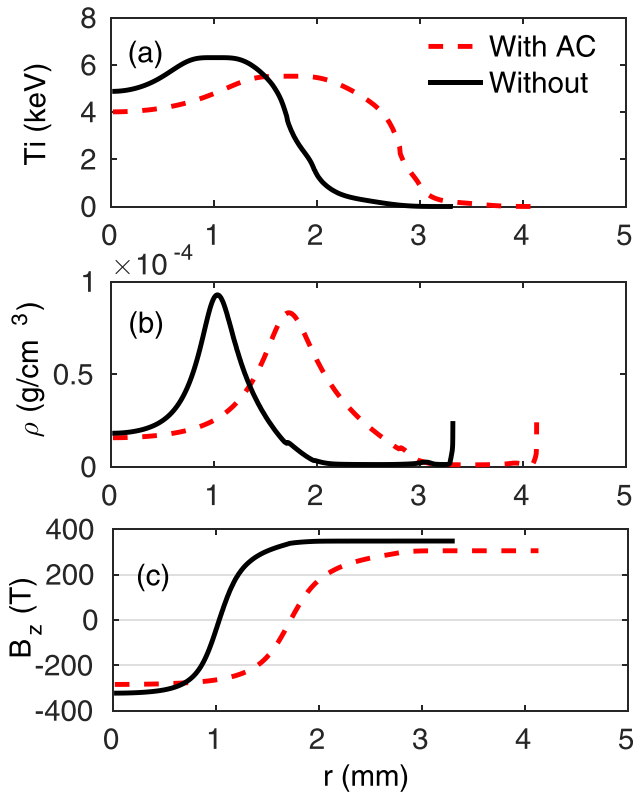


FIG. 11. Other parameters corresponding to case (R, O, Cr, Cz) in Fig. 9, the radial profiles of T_i (a), ρ (b) and B_z (c) at peak compression are plotted for including (red dashed lines) and for not including (black solid lines) the axial contraction (AC), respectively.

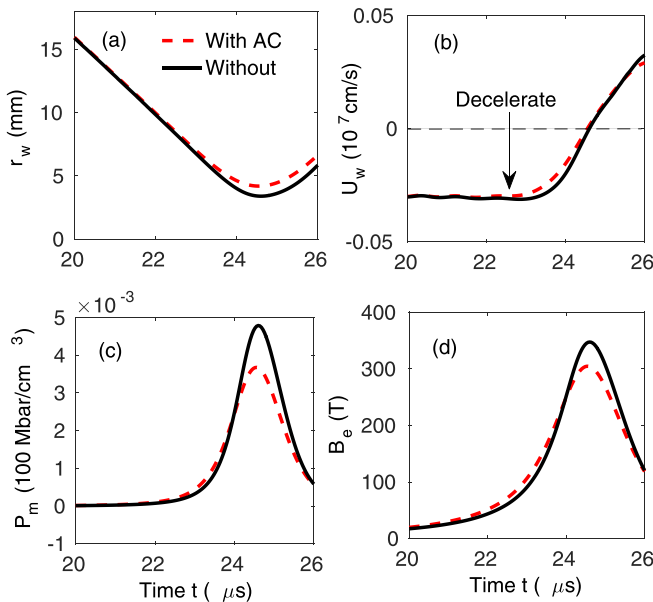


FIG. 12. Corresponding to Fig. 11, the evolution of inner radius of liner r_w , imploding velocity at the inner surface of liner U_w , maximum plasma pressure P_m and external magnetic field B_e as a function of time are shown for cases with (red dashed lines) and without (black solid lines) considering axial contraction (AC), respectively. The plasma pressure and external field are larger for including axial contraction than not including at the initial phase of effective compression of FRCs.

Fig. 12 shows the evolution of inner radius of liner r_w , velocity at the inner surface of liner U_w , maximum pressure P_m and external magnetic field B_e as a function of time corresponding to cases not- (solid line) and including (dashed line) the axial contraction in Fig. 11, respectively. The FRC is compressed and heated effectively when the liner begins to decelerate. It is seen from Fig. 12 that the plasma pressure and external field, which will prevent the imploding liner compressing FRCs, are larger for including axial contraction than not including at the initial phase of effective compression and heating of FRCs, leading to smaller convergence ratio finally. It is inferred that higher initial pressure will decrease the final radial convergence ratio, which is proved by subsequent calculation.

IV. CONCLUSIONS

We propose a one-dimensional physical model for investigating the compression of FRCs by an imploding liner. The effects of axial contraction and parallel thermal conduction are included in the model. The results of this model is consistent with theoretical predictions qualitatively for the adiabatic wall compression of FRCs. The assumption of the rigid-rotor equilibrium model for FRCs is employed in theoretical predictions. In fact, the shape of FRC's profiles cannot keep invariant during implosion, so the evolution of equilibrium may lead to the distinction between simulation and analytical results. But it is found that the profile of plasma will approach to the rigid-rotor equilibrium model if the effects of transport and ohmic heating are included.

The compression work is much larger than the energy loss when the classical transport models are employed inside the separatrix. Consequently, the adiabatic approximation is valid during the axial contraction. Although the adiabatic approximation is violated when the Bohm transport regime dominates, yet it is thought that the drift instabilities leading to anomalous transport may be stable inside the separatrix because of the flat temperature profile.²⁴ Considering the non-physical profile of temperature due to Bohm transport regime, classical transport model is appropriate for the physical model in the MTF regime.

In contrast to expectation, the plasma temperature and density at peak compression phase are a little lower for including the axial contraction motion than not including because of the smaller radial convergence ratio. The effect of axial contraction will increase the plasma pressure and external magnetic at the initial phase of effective compression of FRCs. The increased plasma and magnetic pressure, however, in turn will prevent the imploding liner compressing FRCs, reducing the final radial convergence ratio.

The magnetohydrodynamic instabilities during implosion are not taken into account in the physical model. These instabilities may enhance the thermal conduction and particle flux, even lead to the disruption of FRCs, but these physical mechanisms are beyond the scope of this paper.

ACKNOWLEDGMENTS

Use of code DEIRA (homepage <http://www.basko.net/mm/deira>), built by Prof. Mikhail Basko, is acknowledged.

This work is supported by the National Natural Science Foundation of China (Grant Nos. 11575029 and 11605013).

- ¹M. M. Basko, A. J. Kemp, and J. Meyer-ter-Vehn, *Nucl. Fusion* **40**, 59 (2000).
- ²I. R. Lindemuth and R. C. Kirkpatrick, *Nucl. Fusion* **23**, 263 (1983).
- ³S. A. Slutz and R. A. Vesey, *Phys. Rev. Lett.* **108**, 025003 (2012).
- ⁴I. R. Lindemuth and R. E. Siemon, *Am. J. Phys.* **77**, 407 (2009).
- ⁵R. E. Siemon, P. J. Turchi, D. C. Barnes, and J. H. Degnan, *J. Plasma Fusion Res. Ser.* **5**, 63 (2002).
- ⁶O. V. Gotchev, N. W. Jang, J. P. Knauer, M. D. Barbero, R. Betti, C. K. Li, and R. D. Petrasso, *J. Fusion Energy* **27**, 25 (2008).
- ⁷D. Kirtley and J. Slough, *J. Fusion Energy* **29**, 561 (2010).
- ⁸M. R. Gomez, S. A. Slutz, A. B. Sefkow, D. B. Sinars, K. D. Hahn, S. B. Hansen, E. C. Harding, P. F. Knapp, P. F. Schmit, C. A. Jennings *et al.*, *Phys. Rev. Lett.* **113**, 155003 (2014).
- ⁹P. J. Turchi, *IEEE Trans. Plasma Sci.* **36**, 52 (2008).
- ¹⁰S. C. Hsu, T. J. Awe, S. Brockington, A. Case, J. T. Cassibry, G. Kagan, S. J. Messer, M. Stanic, X. Tang, D. R. Welch *et al.*, *IEEE Trans. Plasma Sci.* **40**, 1287 (2012).
- ¹¹J. H. Degnan, D. J. Amdahl, A. Brown, T. Cavazos, S. K. Coffey, M. T. Domonkos, M. H. Frese, S. D. Frese, D. G. Gale, T. C. Grabowski *et al.*, *IEEE Trans. Plasma Sci.* **36**, 80 (2008).
- ¹²J. Slough, R. Milroy, T. Ziemba, and S. Woodruff, *J. Fusion Energy* **26**, 191 (2007).
- ¹³S. F. Garanin, *IEEE Trans. Plasma Sci.* **26**, 1230 (1998).
- ¹⁴T. Intrator, S. Y. Zhang, J. H. Degnan, I. Furno, C. Grabowski, S. C. Hsu, E. L. Ruden, P. G. Sanchez, J. M. Taccetti, M. Tuszewski *et al.*, *Phys. Plasmas* **11**, 2580 (2004).
- ¹⁵T. P. Intrator, G. A. Wurden, P. E. Sieck, W. J. Wagenaar, L. Dorf, M. Kostora, R. J. Cortez, J. H. Degnan, E. L. Ruden, M. Domonkos *et al.*, *J. Fusion Energy* **28**, 165 (2009).
- ¹⁶J. M. Taccetti, T. P. Intrator, G. A. Wurden, S. Y. Zhang, R. Aragonéz, P. N. Assmus, C. M. Bass, C. Carey, S. A. deVries, W. J. Fienup *et al.*, *Rev. Sci. Instrum.* **74**, 4314 (2003).
- ¹⁷J. H. Degnan, D. J. Amdahl, M. Domonkos, F. M. Lehr, C. Grabowski, P. R. Robinson, E. L. Ruden, W. M. White, G. A. Wurden, T. P. Intrator *et al.*, *Nucl. Fusion* **53**, 093003 (2013).
- ¹⁸R. L. Spencer, M. Tuszewski, and R. K. Linford, *Phys. Fluids* **26**, 1564 (1983).
- ¹⁹T. P. Intrator, R. E. Siemon, and P. E. Sieck, *Phys. Plasmas* **15**, 042505 (2008).
- ²⁰S. Woodruff, A. I. D. Macnab, and N. Mattor, *J. Fusion Energy* **27**, 128 (2008).
- ²¹S. Okada, K. Kitano, H. Matsumoto, K. Yamanaka, T. Ohtsuka, A. K. Martin, S. Yoshimura, S. Sugimoto, S. Ohi, and S. Goto, *Nucl. Fusion* **39**, 2009 (1999).
- ²²F. Conti, F. J. Wessel, M. W. Binderbauer, N. Bolte, F. Giammanco, M. Morehouse, A. Qerushi, H. U. Rahman, T. Roche, and M. Slepchenkov, *Phys. Plasmas* **21**, 022511 (2014).
- ²³D. W. Hewett and R. L. Spencer, *Phys. Fluids* **26**, 1299 (1983).
- ²⁴L. C. Steinhauer, *Phys. Plasmas* **18**, 070501 (2011).
- ²⁵L. C. Steinhauer and T. P. Intrator, *Phys. Plasmas* **16**, 072501 (2009).
- ²⁶S. I. Braginskii, in *Reviews of Plasma Physics*, edited by M. A. Leontovich (Springer, New York, 1965), Vol. 1, p. 205.
- ²⁷M. M. Basko, 2007, see <http://www.basko.net/mm/deira>.
- ²⁸M. M. Basko, P. V. Sasorov, M. Murakami, V. G. Novikov, and A. S. Grushin, *Plasma Phys. Controlled Fusion* **54**, 055003 (2012).
- ²⁹N. A. Bobrova and P. V. Sasorov, *Plasma Phys. Rep.* **19**, 409 (1993).
- ³⁰M. M. Basko, *Nucl. Fusion* **30**, 2443 (1990).
- ³¹W. T. Armstrong, R. K. Linford, J. Lipson, D. A. Platts, and E. G. Sherwood, *Phys. Fluids* **24**, 2068 (1981).
- ³²C. Cereceda, C. Deutsch, M. Peretti, M. Sabatier, M. M. Basko, A. Kemp, and J. Meyer-ter-Vehn, *Phys. Plasmas* **7**, 4515 (2000).
- ³³J. R. Sobehart and R. Farengo, *Phys. Fluids B* **2**, 3206 (1990).